# VISIT Deliverable Report Cover Sheet

| | |
|---|---|
| Workpackage: | WP2: Technical Project Coordination and Development of EOM-BR VCSEL |
| Deliverable number | D2.5a |
| Deliverable name | Unpackaged >40 Gb/s EOM BR VCSEL (including report on design and characterization) |
| Lead beneficiary: | TUB |
| Workpackage leader (name): | VIS |
| Description writer (name): | N. N. Ledentsov |
| Date planned: | 31.10.2011 |
| Date finished: | 10.12.2011 |

Deliverable reached ☒ not reached ☐

Deliverable description and summary of achieved results (max. 2400 char.):

We report the design and characterization of unpackaged EOM BR VCSELs.
The design is strictly Confidential VIS proprietary information. Do not disclose, distribute, or copy. The design is removed for D2.5a.

Contributors:

TUB, VIS, IQE

# VISIT Deliverable Report Technical Annex

| | |
|---|---|
| Deliverable number: | D2.5a |
| Deliverable name: | Unpackaged >40 Gb/s EOM BR VCSEL (including report on design and characterization) |

## Characterization

In Figure 1 we show a schematic cross section of an EOM BR VCSEL. Next in Figure 2 we show another schematic cross section but one that more accurately depicts how the device is fabricated from the epitaxially grown material. In previous EOM BR VCSEL designs we used a true Bragg reflector (BR) design wherein the EOM section lies within a DBR mirror. An alternative design that we used in Project Year 3 is a composite resonator design, wherein the EOM is placed in a second microcavity. A schematic of such a two-resonator cavity EOM BR VCSEL is shown in Figure 3., along with the calculated optical reflectance spectrum.

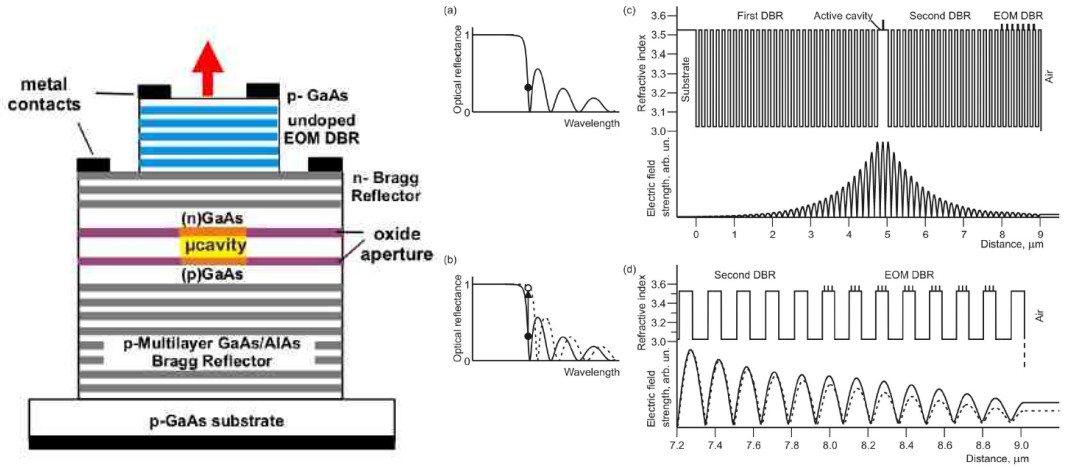


**Figure 1** Schematic diagram of an EOM BR VCSEL (left) and a refractive index profile for the device showing the electric field intensity with and without a bias voltage applied to the EOM section.

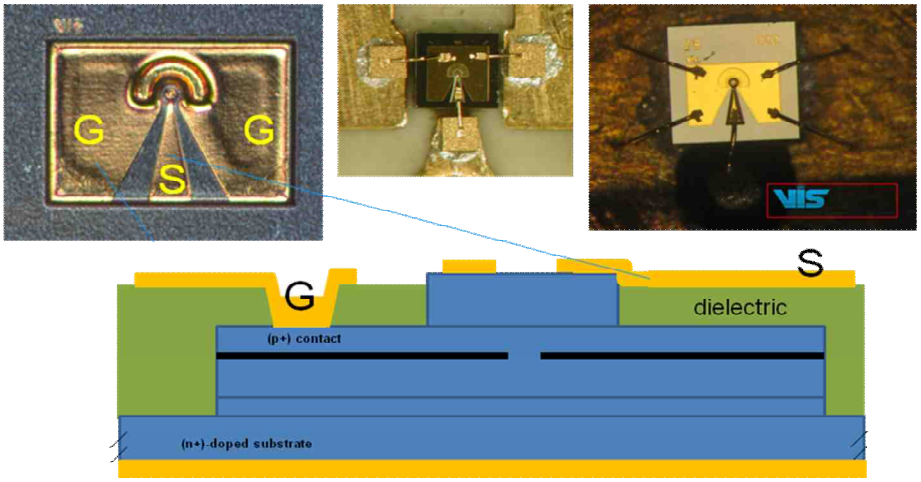


**Figure 2** Schematic diagram of an EOM BR VCSEL indicating the location of the high frequency source (S) and ground (G) contacts with a third contact on the substrate. Also three microscope images of example metal pad configurations matching the intent of the schematic diagram.

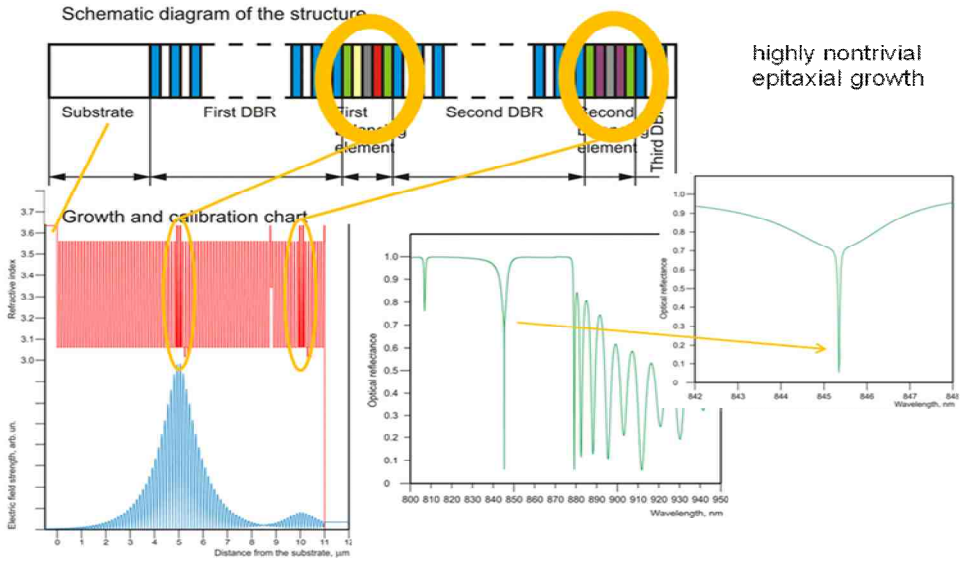


**Figure 3** Schematic diagram of an Gen 2 EOM VCSEL in the form of a composite resonator.

A structure based on a composite resonator EOM VCSEL design was given to IQEe for epitaxial growth and included oxide aperture layers in both the VCSEL and the EOM sections with the intention to reduce mesa capacitance and thus increase the device's bandwidth. The partners discussed in great detail the epitaxial device design, the growth parameters, and a growth strategy including a set of calibration structures. With this detailed information IQE completed the growth of EOM BR VCSEL #4. The measured optical reflectance for this structure is shown in Figure 4.

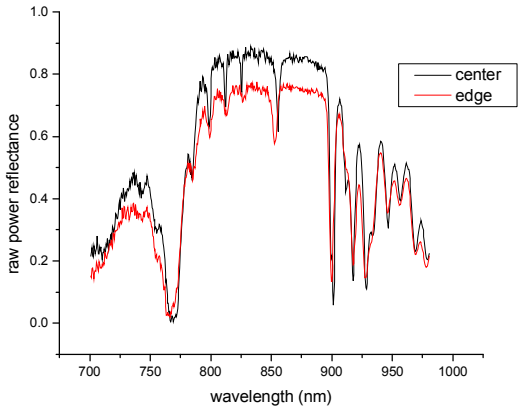


**Figure 4** Measured optical reflectance of EOM BR VCSEL #4 in two wafer substrate locations after growth by MOVPE by IQEe.

Similarly VIS designed two other composite resonator EOM BR VCSEL structures for growth by MBE via the planned subcontract with IQE Inc. (USA). IQE Inc. Successfully grew these two other Gen 2 EOM BR VCSEL structures and the measured optical reflectance is given in Figure 5.

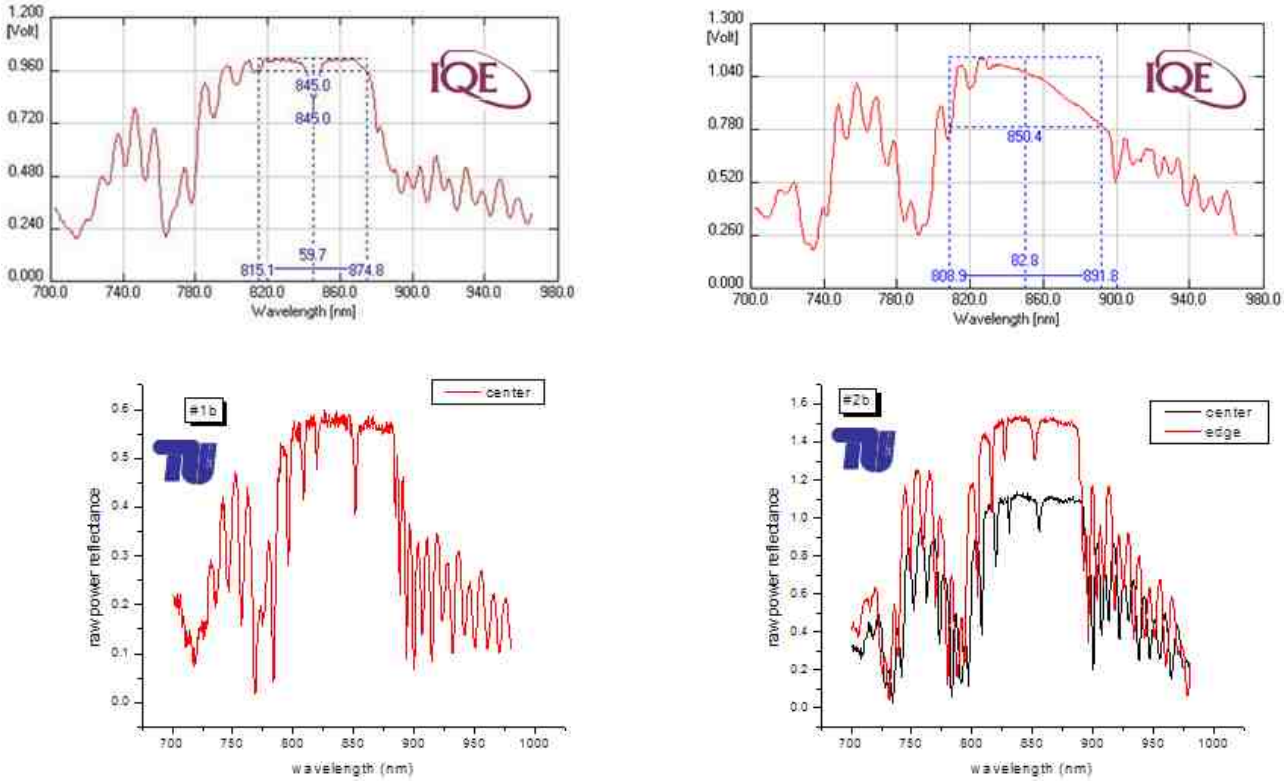


**Figure 5** Measured optical reflectance of EOM BR VCSEL #1b and #2b in after growth by MBE by IQE Inc. (USA).

Using a new EOM BR VCSEL mask set (designed and produced by TUB) TUB performed a series of processing development steps seeking to successfully produce EOM BR VCSELs from the epitaxial wafers. A comparison of the MOVPE-grown Gen 1 and Gen 2 EOM BR VCSELs after oxidation of

the aperture layers is shown in Figure 6. Subsequently the TUB was closed from January through September for renovation work and it was not possible to continue processing additional EOM BR VCSEL material. As a result, the partners instead performed an analysis and further testing of the EOM BR VCSEL #3 structure that has been processing in Project Year 2.

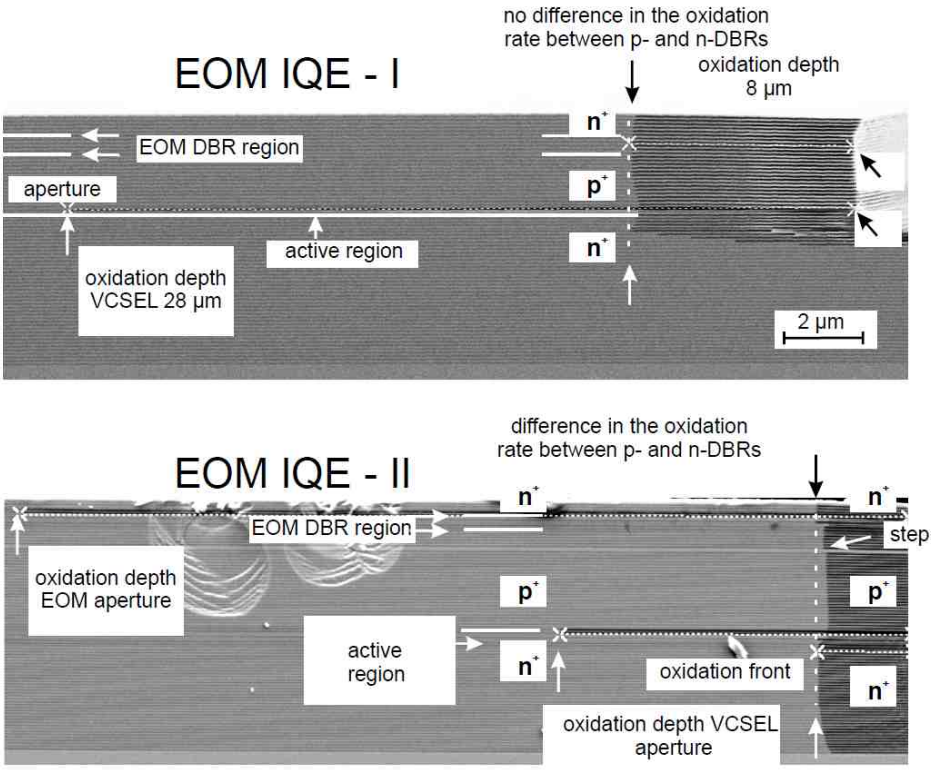


**Figure 6** Scanning electron micrographs of EOM BR VCSEL #3 (top) and #4 (bottom).

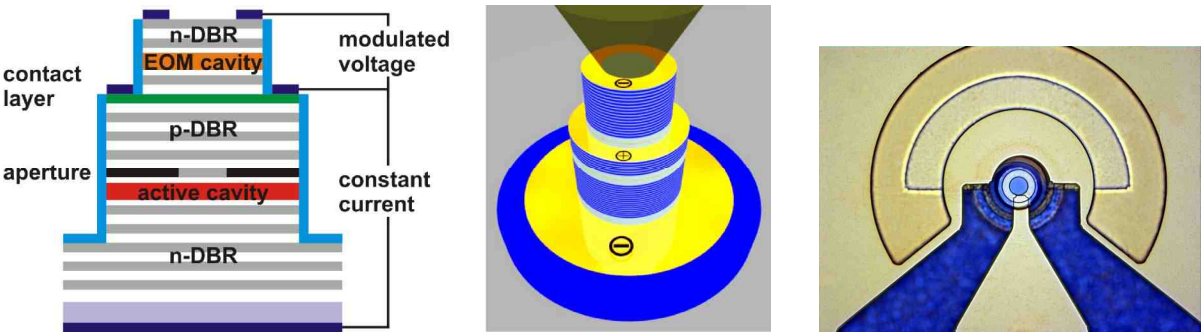


**Figure 7** Schematic diagram of an EOM BR VCSEL for use in device modelling (left and center), and a top down white light microscope image of an actual TUB-processed EOM BR VCSEL using a new mask set created for this purpose (right).

## Electro-Optical Resonance Modulation of VCSELs

Optical and electrical investigations of vertical-cavity surface-emitting lasers (VCSEL) with a monolithically integrated electro-optical modulator (EOM) allow for a detailed physical understanding of this complex compound cavity laser system. The EOM VCSEL light output is investigated to identify optimal working points. An electro-optic resonance feature triggered by the quantum confined Stark effect is used to modulate individual VCSEL modes by more than 20 dB with an extremely small EOM voltage change of less than 100 mV. Spectral mode analysis reveals modulation of higher order modes and very low wavelength chirp of < 0.5 nm. Dynamic experiments and simulation predict an intrinsic bandwidth of the EOM VCSEL exceeding 50 GHz.

**EOM-VCSEL device concept**

The device concept of the present EOM VCSEL aims at the monolithic integration of a modulator with a VCSEL to benefit from the established fabrication and processing technologies and match the industry-relevant 850 nm wavelength range. Initial results of this device were published in references. Figure 7 shows schematics of the device depicting a third electric middle-contact. Compared to a conventional VCSEL this additional contact electrically divides the device into two sections: at the basis a VCSEL and on top the EOM section realized as a second cavity within the VCSEL top DBR. All DBRs consist of $Al_{0.9}Ga_{0.1}As$ and $Al_{0.15}Ga_{0.85}As$ □/4 layers employing graded interfaces with doubled doping levels to facilitate charge carrier transport within the device.

A conventional design with a GaAs MQW gain-medium with $Al_{0.2}Ga_{0.8}As$ barriers is chosen for the VCSEL section. Adjacent to the active cavity within the first DBR pair an AlAs layer enclosed by AlGaAs-gradings is introduced for post-growth oxidation of a crack-free aluminum-oxide current-aperture using TUB's novel oxidation technology. The bottom high-reflectivity AlGaAs DBR is n-doped while the intermediate DBR between active-cavity and EOM-cavity is p-doped. Within this p-doped DBR a lattice matched InGaP layer adjacent to a *p*+-doped GaAs contact layer serves as etch-stop during processing of the middle-contact. Active QW spectral position is confirmed to be at 835 nm wavelength by photoluminescence characterization while InGaP lattice matching is verified by X-ray diffraction measurements.

The EOM section starts on top of the middle-contact layer with the remaining part of the p-DBR. To employ the quantum-confined Stark effect for light output modulation an undoped cavity is formed by a GaAs MQW stack with $Al_{0.2}Ga_{0.8}As$ barriers. These EOM QWs are spectrally shifted towards shorter wavelengths with respect to the active VCSEL. On top of the EOM-cavity a Si-doped 10x DBR with a GaAs cap layer protecting against oxidation finalizes the structure. Spectral positioning of emission wavelength and EOM QWs aims at a minimized absorption within the EOM element while maintaining a sufficient refractive index modulation referred to as region II in reference. Consequently EOM QWs are tuned to a higher energy with respect to the active QWs of the VCSEL section. The EOM principles of the VCSEL output are described as follows. According to the Kramers-Kronig relation, the change of the complex refractive index of the EOM-QW section by applying an electric field is due to both the spectral shift of the QW absorption peak as well as the change in oscillator strength of the excitonic absorption. Thus, both the absorption strength as well as the EOM-cavity resonance-wavelength is changed. If the VCSEL-cavity resonance wavelength is close to the EOM-cavity resonance wavelength the latter becomes significant. Our EOM-VCSEL design is targeted at working under resonance condition.

Prior to the final prototype, test samples are grown and investigated to tune and optimize all parts of the device individually. DBR stop band reflectivity and cavity spectral position are determined by surface reflectivity measurements and compared well with transfer matrix simulations. A single growth run is performed to grow the entire monolithic EOM VCSEL at 680°C using metal-organic vapor phase epitaxy. Temperature is solely lowered to 595°C for the deposition of the lattice matched InGaP etch-stop layer which is covered with 5 nm of GaAs prior to heating up again to resume DBR growth. A horizontal flow Aixtron 200/4 reactor equipped with TMIn, TMGa, TMAl, TBP and arsine precursors is used yielding excellent uniformity on 2-inch GaAs:Si (1 0 0) substrates for the whole structure comprising close to 400 layers. Optical reflectance and reflectance anisotropy are recorded in-situ by an optical sensor to monitor DBR growth stability and process cycles. Employing standard lithography and dry etching techniques devices are processed with varying mesa diameters from 25 to 36 µm and 45 to 56 µm for EOM and VCSEL sections, respectively. Selective oxidation of the Al-rich aperture layer is realized using optimized conditions. Three ohmic contacts are realized for device operation, bottom and middle contact for the VCSEL part, middle and top contact for the EOM part.

**Static Characteristics**

Dynamic and static characteristics are investigated at room temperature (RT) with operational devices mounted on a copper heat-sink. For all measurements the VCSEL section is driven at constant current above lasing threshold to enable CW emission. Modulation of the optical output is realized solely by applying a reverse EOM-voltage. The current flow across the EOM section is monitored simultaneously as a measure for the photo-absorption of laser emission within the modulator. Fundamental laser characteristics and the corresponding EOM photocurrent of a multi-mode device with 28 µm EOM mesa-diameter are given in Figure 8. Data show a constant lasing threshold independent of the applied reverse EOM bias indicating good optical modulator isolation from the VCSEL section.

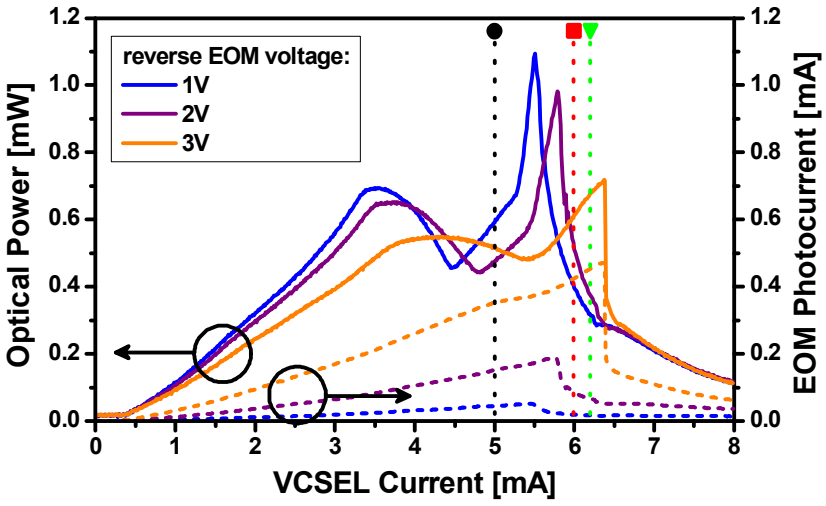


**Figure 8** Solid lines: Optical output power characteristics of the EOM VCSEL are shown for different voltages applied to the EOM section. Dashed lines: Corresponding photocurrent due to absorption within the EOM section. Dotted lines: Guides to the eye identify the position of data.

Optical output-power and EOM photocurrent increase linearly with the VCSEL drive current up to about 3.3 mA. With increasing EOM reverse bias, however, the absorption increases and the output power decreases. Within this current range, modulation of the VCSEL output is thus primarily due to change of absorption strength in the EOM section. Upon further increase of VCSEL current, the optical output power is decreasing, likely limited by thermal rollover. Within a current range of 5 to 6.5 mA, the VCSEL output power increases again but strong superlinearly. Up to the narrow output peak maximum at resonance the photocurrent increases linearly and then drops sharply. Upon further increased current both values finally decrease. The second optical output power increase cannot be explained by a change of absorption within the EOM section. Instead, we attribute this feature to resonance matching of the two coupled cavities within the device. For devices sharing a similar cavity design, a resonant output power behavior is typical. We analyze the dynamics after we derive a qualitative explanation for the observed resonance peak.

For larger EOM reverse bias, the energy of the exciton absorption peak is decreased but the refractive index change can be positive or negative thus the resonance wavelength of the EOM cavity is altered depending on device properties. Our EOM cavity resonance at zero bias is set to a slightly longer wavelength with regard to the VCSEL resonance and the energetic separation between both cavity resonances is increased by a larger reverse bias. This increase is counter-balanced by increasing the VCSEL current. The intrinsic temperature and subsequently the effective refractive index of the VCSEL section are both increasing due to heating. The resonance wavelength shift of both cavities depends on their spectral resonance positions controlled (amongst others) by the corresponding effective refractive indices. The refractive index change of the EOM MQW due to the quantum-confined Stark-effect is rather limited ($\Delta n \approx 0.01$). Thus resonance modulation requires precise matching of the cavity resonances and definition of the correct operating point of the device. For our structure, the separation of the resonances is designed and experimentally observed to be only 1 nm. Reflection spectra of test samples containing the individual cavity structures and the final EOM VCSEL together with fits using the transfer matrix method are used.

**Resonance Analysis**

To distinguish between absorption related and index of refraction induced resonance effects on signal modulation we analyze now in more detail the output power and the photocurrent within the 1-3 V EOM bias range as a function of the VCSEL drive current (see Figure 9). Additionally this figure includes the sum of both values (the EOM photocurrent is converted to the corresponding optical output power at the wavelength of operation) giving the total output power $P_{tot}$ of the VCSEL section. $P_{tot}$ shows an almost flat behavior for 5 mA (black curve, bottom viewgraph). Thus, the modulation of the light output as seen in the center of the figure is solely driven by absorption within the EOM section and a rather large EOM voltage sweep of 1.5 V is necessary to realize 3 dB optical intensity modulation. At higher VCSEL drive currents of 6.0 and 6.2 mA (red and green curves) a sudden increase of the output power is revealed. Upon a voltage change of less than 100 mV $P_{tot}$ almost doubles and only a fraction of this increase is due to absorption in the EOM section. This step like increase of the total VCSEL output power directly proves the onset of coupling between the two cavities: the EOM resonance wavelength is varying as a function of voltage. This steep increase of optical output power at resonance represents a very efficient modulation of the device. We call this electro-optic resonance modulation (ERM).

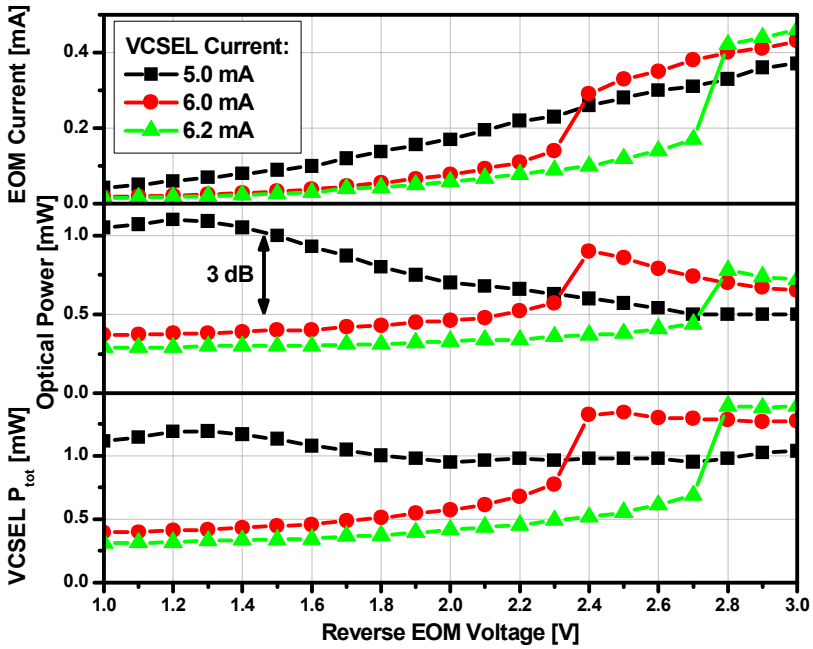


**Figure 9** Top: Directly measured EOM photocurrent Center: Integral optical output power. Bottom: Total VCSEL section output (EOM absorbed power + optical output power) - Data for three different currents of the VCSEL section are plotted. 5.0 mA shows a flat $P_{tot}$ behavior while 6.0 mA and 6.2 mA drive currents show distinct resonance behaviors upon EOM voltage change doubling the total VCSEL output $P_{tot}$. This simultaneous increase of optical output power and EOM photocurrent is attributed to the resonance of both cavities due to EO-effect induced changes.

For our mesa diameter of 28 µm and current aperture diameter of 5 µm the device shows four significant transverse modes. The impact of the ERM on individual modes is analyzed using an optical spectrum analyzer.

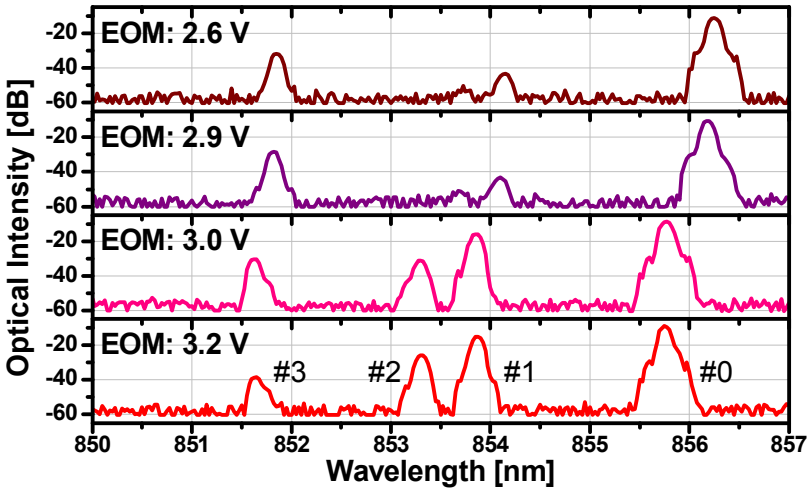


**Figure 10** Modes of the EOM VCSEL at RT. Drive current of the VCSEL section is kept constant for all curves at 6.2 mA while the EOM voltage is varied from 2.6 V to 3.2 V. Significant changes due to the onset of the compound cavity resonance are found upon a change of only 100 mV from 2.9 to 3.0 V.

Figure 10 shows the fundamental mode (#0) at 856.2 nm and three higher order modes numbered (#1-3) at shorter wavelengths for bias values between 2.6 and 3.2 V. Between 2.9 V and 3.0 V the intensities of the 1st and the 2nd modes are increasing by 20 dB and 27 dB, respectively. The wavelength of all modes shifts by less than 0.5 nm upon this bias change involving ERM.

Previous large-signal experiments on similar devices revealed a limited modulation bandwidth of 3 GHz. Here we present a small-signal analysis to investigate the origin of this bandwidth limitation. Opposite to conventional current modulated devices the small-signal modulation transfer function of photon lifetime $\tau_p$ modulating devices decreases with $1/\omega$ instead of $1/\omega^2$. For this investigation the device is biased ensuring resonance conditions. Direct measurements of the small-signal modulation bandwidth ($S_{21}$) identify tight limitations with a sharp drop at the beginning of the frequency range. As this is usually an indication of a parasitic limit, we conducted a more detailed investigation of the device impedance ($S_{11}$). The results of this investigation are presented in Figure 11.

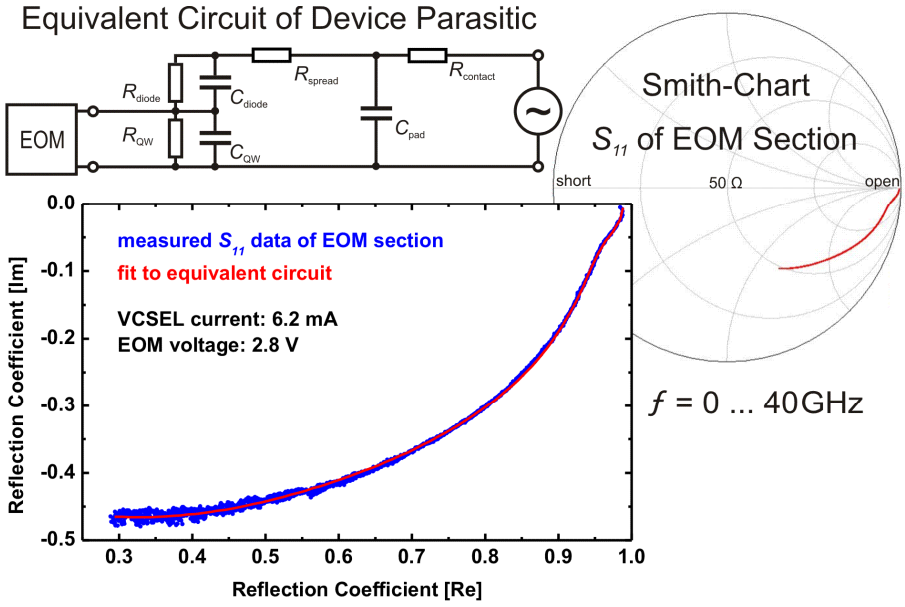


**Figure 11** Smith Chart of electrical impedance ($S_{11}$) of EOM-section between 0…40 GHz and equivalent circuit of parasitic network. The intrinsic (ideal) EOM-section is represented as a two pole square being connected to a parasitic network. Drive current of the VCSEL section is 6.2 mA, EOM voltage is 2.8 V.

The EOM-section is modeled as reverse-biased PIN-diode and the parasitic device values can be extracted with high accuracy. We split the EOM-section into the diode capacitance of the space-charge regions of the *p*- and *n*-side (which can be modeled as one lumped element $C_{diode}$) and an additional capacitance $C_{QW}$ from the EOM QWs only. Each of these capacitors has a leakage resistance $R_{diode}$ and $R_{QW}$, respectively. Additionally we found a spreading resistance $R_{spread}$ caused by the surrounding cladding layers, a pad capacitance $C_{pad}$ and a non-perfect contact resistance $R_{contact}$. The response from the parasitic equivalent circuit perfectly describes the measured $S_{11}$-values across the entire (setup-limited) frequency range from 0 to

40 GHz. Changes of device values are also consistent with changes of the EOM-voltage. The lumped element values for different EOM-voltages are given in Table 1.

| $U_{EOM}$ | $C_{QW}$ | $R_{QW}$ | $C_{diode}$ | $R_{diode}$ | $R_{spread}$ | $C_{pad}$ | $R_{contact}$ |
|---|---|---|---|---|---|---|---|
| **2.8 V** | 55 fF | 1040 Ω | 177 fF | 6.5 kΩ | 309 Ω | 55.4 fF | 35.9 Ω |
| **3.0 V** | 56 fF | 940 Ω | 176 fF | 8.1 kΩ | 308 Ω | 55.3 fF | 35.9 Ω |
| **3.2 V** | 60 fF | 650 Ω | 173 fF | 10 kΩ | 302 Ω | 55.4 fF | 35.9 Ω |

**Table 1** Fitting values of the equivalent circuit of the parasitic network (as shown in figure 5). The values are derived from EOM VCSEL $S_{11}$ measurements at RT for different EOM-voltages. Drive current of the VCSEL section is 6.2 mA.

For increasing voltage, the space-charge capacitance $C_{diode}$ decreases consistently with the increase of the depleted region. As expected the corresponding leakage resistance $R_{diode}$ becomes significantly larger. The outer parasitic network is practically invariant to changes in voltage, whereas the EOM-section itself varies its impedance significantly. With increasing photo-current (compare Figure 9) the leakage resistance $R_{QW}$ decreases, while the capacitance $C_{QW}$ becomes larger due to the variation of the refractive index and photo-absorption induced heating. From this equivalent circuit model we can extract the parasitic response of the EOM-section which is clearly limiting the high-speed performance of our prototype device. Extraction of the parasitic response by means of fitting from the $S_{21}$-curve yields very similar results.

$$S_{21}(\omega) \propto \frac{1}{\tau_p} \cdot \frac{\omega_0^2 \tau_p + j\omega}{\omega_0^2 - \omega^2 + j\omega\gamma} \qquad (1)$$

The parasitic limited performance of the device is also in agreement with our estimates based on device geometries and doping levels. To determine the intrinsic device speed with resonance conditions the parasitic response is deconvoluted from the measured frequency response. The intrinsic device speed can be fitted to Eq. (1). This fit yields a photon lifetime $\tau_p$ of 4.1 ps, a resonance-frequency $\omega_0$ of $2\pi \cdot 27$ GHz and a damping coefficient $\gamma$ of 1.5 $10^{11}$ $s^{-1}$ at driving conditions of 6.2 mA and 2.8 V. The result is depicted in Figure 12, predicting an intrinsic device bandwidth of 56±5 GHz.

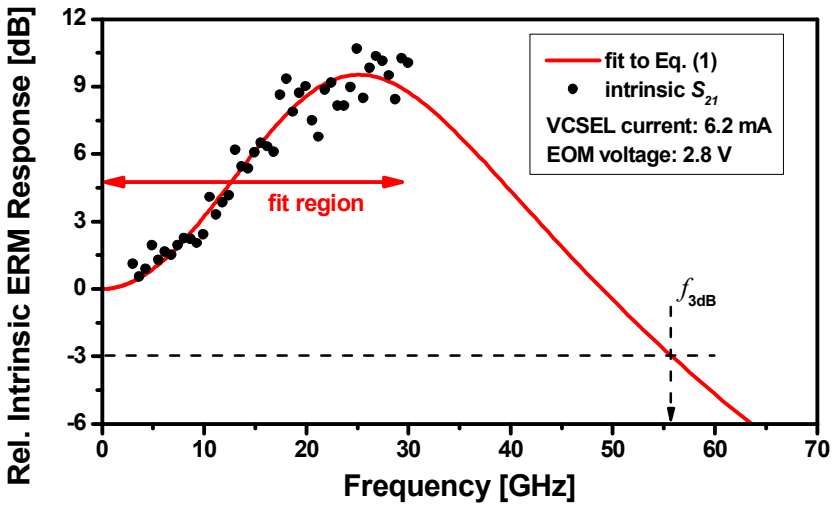


**Figure 12** Intrinsic bandwidth of the EOM VCSEL at RT. Electrical parasitics are deconvoluted from the measured data yielding an intrinsic bandwidth of 56±5 GHz.

Such a bandwidth together with a large overshoot is typical for intra-cavity loss modulated lasers. A well-tailored parasitic response is needed to flatten out the characteristic overshoot in the device response without limiting the bandwidth. Therefore, a detailed knowledge about the parasitic network of the chip as presented in Figure 11 is crucial. Due to similar confinement factors the resonance frequencies of common laser diode designs tend to saturate at some 20-30 GHz limiting the device bandwidths to some 40 Gbps. Optically isolated external modulators can overcome these limitations at the expense of a more complex system layout connected with higher cost and energy consumption. Intra-cavity loss-modulated devices, especially EOM-VCSELs, can thus overcome the bandwidth limitation of directly modulated laser diodes at the low manufacturing costs of a conventional VCSEL.

Future EOM VCSEL generations will reduce the large parasitics of this prototype by employing smaller EOM mesa diameters and additional oxide apertures for the EOM part. Additionally, efficient modulation could necessitate single mode operation. The modulation depth of the EOM cavity can be improved by employing a larger numbers of QWs, which are precisely tuned to minimize absorption while maintaining sufficient refractive index modulation. Additionally high bandwidth device processing and mounting is required to reduce the external parasitics.

**Conclusions**

Modulation characteristics of a monolithic EOM VCSEL are analyzed and absorption and refractive index changes are separately investigated in detail. We find strong electro-optic resonance modulation (ERM), where the light output of the device is modulated by changing the coupling between the two integrated cavities. This allows for ultra-low voltage modulation with a swing of less than 100 mV for optical amplitude changes up to 27 dB. Determination of the equivalent circuit diagram of the parasitics and deconvolution results in a record high intrinsic bandwidth of the EOM VCSEL of 56 GHz. Thus data rates of close to 100 Gbit/s seem to be feasible with technologically improved devices.